ADVANCED FUNCTIONAL MATERIALS
www.afm-journal.de

Reversible Colossal Barocaloric Effect of a New Fe^{II} Molecular Complex with Low Hysteretic Spin Crossover Behavior

Maksym Seredyuk, Ruixin Li, Kateryna Znovjyak, Zhe Zhang, Francisco Javier Valverde-Muñoz, Bing Li,* M. Carmen Muñoz, Quanjin Li, Bingbing Liu, Georgiy Levchenko,* and José Antonio Real**

Barocaloric cooling, that is, lowering the temperature of a material under pressure action, is an attractive solid-state effect that can potentially compete with volatile gas-based cooling. To observe the barocaloric effect (BCE), it is necessary for materials to have high-entropy, low-hysteretic phase transitions with a large volume change between phases. Here details on a new Fe^{II} complex $[Fe(L)(NCS)_2]$, L = N^1,N^3-bis((1-propyl-1*H*-1,2,3-triazol-4-yl) methylene)-2,2-dimethylpropane-1,3-diamine) possessing spin crossover (SCO) behavior near room temperature with large entropy and volume change are reported, which provides high sensitivity to external pressure. The observed BCE effect, characterized using variable pressure calorimetry, powder X-ray diffraction, UV–vis, IR, and Raman spectroscopy, shows a colossal isothermal entropy change of >100 J kg^{-1} K^{-1} and a reversible adiabatic temperature change of ≈16 K at a pressure of 1 kbar, demonstrating a high refrigerant efficiency compared to other solid-state materials. These results stimulate further investigations of SCO materials as barocaloric refrigerants, which depend on the proper design of their constituent organic ligands.

1. Introduction

Currently, the need for cooling is ubiquitous in life and industry, and the annual electricity consumption of the refrigeration industry accounts for about one-fifth of the global electricity supply.[1] With the rapid development of society and economy, this proportion will be further increased. For example, energy consumption for air conditioning and cooling will triple by mid-century.[2] The work of these refrigeration units is primarily based on the cyclic compression of volatile hydrofluorocarbon refrigerants, some of that are commonly used and have a global warming potential 1000–2000 times that of carbon dioxide.[3] Although steam compression technology is well developed and efficient, there is a lack of energy-saving and environmentally friendly refrigerants. Therefore, the search for efficient and

M. Seredyuk, K. Znovjyak
Department of Chemistry
Taras Shevchenko National University of Kyiv
Kyiv 01601, Ukraine
E-mail: maksym.seredyuk@knu.ua
M. Seredyuk, F. J. Valverde-Muñoz, J. A. Real
Instituto de Ciencia Molecular
Universidad de Valencia
Catedrático José Beltrán 2, Paterna 46980, Spain
E-mail: jose.a.real@uv.es

The ORCID identification number(s) for the author(s) of this article can be found under https://doi.org/10.1002/adfm.202315487

DOI: 10.1002/adfm.202315487

M. Seredyuk
Enamine Ltd.
Winston Churchill Str. 78, Kyiv 02094, Ukraine
R. Li, Q. Li, B. Liu, G. Levchenko
State Key Laboratory of Superhard Materials
International Centre of Future Science
Jilin University
Changchun 130012, China
E-mail: g-levch@ukr.net
Z. Zhang, B. Li
Shenyang National Laboratory for Materials Science
Institute of Metal Research
Chinese Academy of Sciences
72 Wenhua Road, Shenyang, Liaoning 110016, China
E-mail: bingli@imr.ac.cn
Z. Zhang, B. Li
School of Materials Science and Engineering
University of Science and Technology of China
72 Wenhua Road, Shenyang, Liaoning 110016, China

ecological refrigerants is urgent, which also promotes the research of sustainable alternative refrigeration technologies.[4]

The most promising alternative cooling techniques are based on the caloric effects of solid materials with reversible phase transitions,[5] resulting in isothermal entropy changes and adiabatic temperature changes through the application and removal of external fields. The caloric effect of solid materials can be classified into magnetocaloric, electrocaloric, and mechanocaloric, depending on the external stimuli applied, specifically the magnetic field, electric field, or mechanical stress.[6] BCE is a subtype of mechanocaloric effects observed under hydrostatic pressure as an external stimulus.[6e,7] Compared with other thermal effects, barocaloric materials are less prone to fatigue in the cycle, and the device for generating hydrostatic pressure is simpler, which will reduce costs for large-scale applications.[8] Moreover, a colossal and reversible BCE can be produced at a low pressure (<0.1 kbar), comparable to the thermal effect induced by a considerable electric or magnetic field. This has sparked interest in BCE as an alternative to vapor-compression technologies because it is more common than other thermal effects and, in fact, arises from the relationship between a certain degree of freedom in the organization of lattice components and the volume change of the material.[6e,7] Excellent BCE is expected for materials with large volume and entropy changes undergoing abrupt transitions. Yet, most abrupt phase transitions are usually accompanied by a large hysteresis width,[9] which leads to the need for increased pressure to realize a reversible cycle and reduces the cooling efficiency compared to non-hysteretic barocaloric materials.[10] Therefore, it is necessary to search for phase transition materials in which hysteresis is absent or has a small hysteresis loop width.

In 2016, the spin crossover (SCO) behavior was first proposed as a promising mechanism for inducing the BCE, and was investigated theoretically and experimentally in the following years.[11] The SCO phenomenon is generally observed in coordination compounds with octahedral coordination environments for *3d*-transition metal ions. For example, Fe^{II} SCO compounds transform between diamagnetic-low spin (LS, $S = 0$) and paramagnetic-high spin (HS, $S = 2$) electron configurations under external stimuli (temperature, pressure, and light). The thermally induced transformation of enthalpy-favored LS at low-temperatures into entropy-favored HS at high-temperatures is usually accompanied by a significant increase in entropy due to an increase in the electronic and vibrational degrees of freedom of matter.[12] Since the SCO behavior is accompanied by expansion/contraction of the unit cell volume caused by a substantial change in the Fe^{II} polyhedron, the transition exhibits high sensitivity to external pressure according to the Clausius–Clapeyron equation ($\frac{dT_{1/2}}{dP} = \frac{\Delta V}{\Delta S}$). In particular, any compound exhibiting first-order SCO behavior will be suitable for low-pressure and high-efficiency barocaloric refrigeration.[10] The study of the BCE of SCO materials is at an early stage, and only three SCO compounds have been directly characterized by high-pressure calorimetry,[11d–f] therefore it is highly relevant to further search for SCO materials for the field of solid refrigeration. In this context, an ideal barocaloric SCO compound for application at room temperature should have a sharp non-hysteretic transition just below RT with a large entropy gain and a large unit cell volume change. These requirements severely limit the number of suitable types of SCO compounds. For example, the two low-hysteretic barocaloric SCO compounds described so far show a transition above RT,[11e,f] and are not suited for ambient conditions, therefore the search for SCO materials for real-world applications continues.

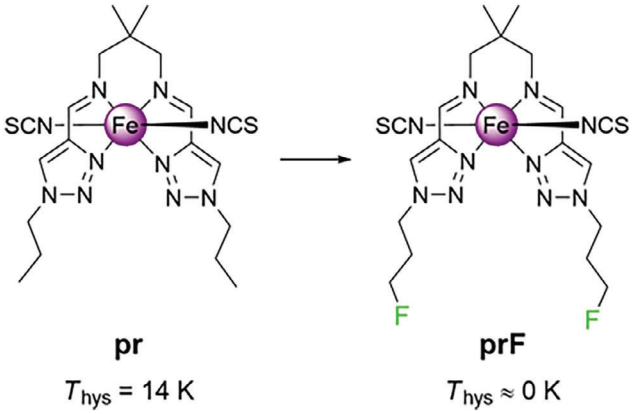

Scheme 1. Molecular structure of **pr**[14c] and **prF**.

The pressure sensitivity of SCO compounds is consistent with Le Chatelier's principle, which states that the larger the change in material volume during SCO, the lower the pressure must be to actuate a reversible pressure-driven transition. Usually, the volume of the SCO compounds changes in the range of 1–5% and is higher for compounds with smaller ligand molecules.[13] To this end, an attractive class of SCO compounds is represented by thiocyanate Fe^{II} complexes, $[FeL(NCS)_2]$, based on a new type of tetradentate ligands, obtained by condensation of *N*-substituted 1,2,3-triazolecarbaldehydes, and 2,2-dimethyl-1,3-diaminopropane.[14] Depending on the substituents introduced into the triazole moieties, the complexes can remain HS[15] or exhibit SCO in a 200–400 K range with varied hysteresis width as demonstrated on a series of complexes with aliphatic and aromatic groups.[14] Since non-hysteretic or low-hysteretic transition is a key property for the realization of an effective BCE, it is essential to minimize the loop width that can be achieved by utilizing chemical design principles. Accordingly, we have proceeded from the idea that by the fluorination of the peripheral groups of the recently reported complex **pr** (**Scheme 1**, L = *N*,^{1}*N*^{3}-bis((1-propyl-1*H*-1,2,3-triazol-4-yl)methylene)−2,2-dimethylpropane-1,3-diamine) and anchoring in this way aliphatic chains by F—X supramolecular bonding can potentially inhibit the symmetry-breaking phase transition that

F. J. Valverde-Muñoz
CNRS
IPR – UMR 6251
Univ Rennes
Rennes F-35000, France
M. C. Muñoz
Departamento de Fisica Aplicada
Universitat Politècnica de València
Camino de Vera s/n, Valencia 46022, Spain
G. Levchenko
Donetsk Physical-Technical Institute named after A. A. Galkin NANU
Kyiv 03028, Ukraine

accompanies the SCO transition in this compound, resulting in a large hysteresis loop of ≈14 K.[14c] At the same time, the closest van der Waal's radii between H and F atoms and bond length with carbon can ensure the minimum disruption of the crystal structure due to steric hindrance. Indeed, by introducing terminal fluorine atoms into the propyl pendants, the **prF** complex was obtained (Scheme 1, L = *N*,$^1N^3$-bis((1-(3-(3-fluoropropyl)−1*H*-1,2,3-triazol-4-yl)methylene)−2,2-dimethylpropane-1,3-diamine), which inherits the high entropy gain and transition temperature below RT of the parent complex **pr**, but possesses a key small width hysteresis that allows to exhibit a colossal BCE, as follows from the exhaustive structural, magnetic, calorimetric, and spectroscopic studies presented below.

2. Results

2.1. Synthesis, Structure, and Thermal-Induced SCO Behavior at Ambient Pressure

2.1.1. Synthesis

The derivative 1-(3-fluoropropyl)−1,2,3-triazole-4-carbaldehyde was prepared from commercially available 1-azido-3-fluoropropane according to the one-pot click reaction protocol by Fletcher et al.[16]Subsequently, the tetradentate ligand was prepared in situ by the condensation reaction with 2,2-dimethyl-1,3-propanediamine, which further reacted with $[Fe(py)_4(NCS)_2]$ in methanol and produced the desired complex **prF** in the form of needle-like crystals (for detail see the Supporting Information). The complex demonstrates thermochromism from orange-red at RT to dark red-violet upon moderate cooling.

2.1.2. Magnetic and Thermal Properties at Atmospheric Pressure

The magnetic curve of **prF** at a rate of 1 K min^{-1} and in the form of $\chi_M T$ versus T plot is shown in **Figure 1** (χ_M is the molar magnetic susceptibility and T the temperature). At 400 K, the $\chi_M T$ reaches the value 3.55 cm^3 K mol^{-1} that is consistent with the Fe^{II} centers in the HS state. Upon cooling, starting from 350 K, $\chi_M T$ first gradually reduces to 2.90 cm^3 K mol^{-1} and then drops rapidly within a few Kelvin to 0.70 cm^3 K mol^{-1} with $T_{1/2}$ = 270 K and continues to decrease to reach values close to zero at *ca.* 200 K, that is consistent with a fully populated LS state ($T_{1/2}$ is temperature where %(LS) = %(HS) = 50%). In the heating mode, the $\chi_M T$ values match those of the cooling mode showing the absence of hysteresis.

The heat capacity trace of **prF** at 10 K min^{-1} has a peak at 267 K on heating and a peak at 265 K on cooling, revealing a small hysteresis 2 K wide at this scan rate (Figure 1). The average enthalpy and entropy values are 13.3 kJ mol^{-1} and 49.7 J K^{-1} mol^{-1} (89.9 J K^{-1} kg^{-1}), respectively, and are characteristic of the cooperative Fe^{II} systems.[17] The entropy value is significantly higher than expected from electronic considerations (spin degeneracy only: $^1A_1 \rightarrow {}^5T_{2g}$ transition, $\Delta S_{elec} = R\ln(5) = 13.4$ J K^{-1} mol^{-1}). The remaining entropy variation (49.7–13.4 = 36.3 J K^{-1} mol^{-1}) accounts for the crystal and molecular vibrational modes involved in the ST process. Fitting the SCO transition curve with the Slichter–Drickamer model[18] with the entropy and enthalpy fixed to the experimental values, result in the cooperativity parameter Γ = 4.5 kJ mol^{-1} (Figure S1, Supporting Information).

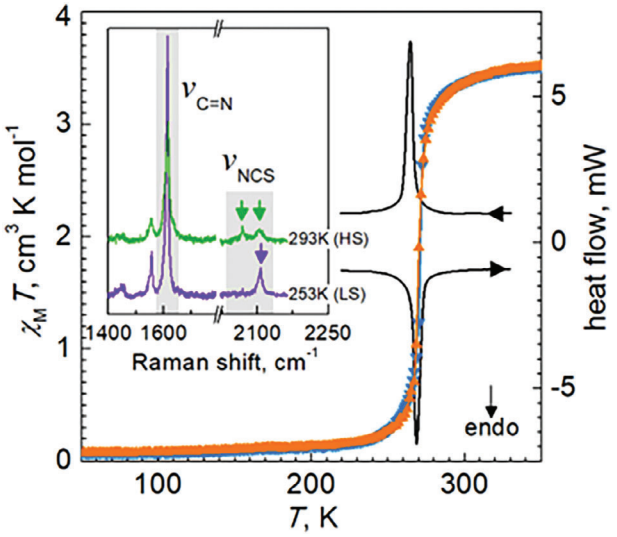

Figure 1. Plot $\chi_M T$ versus T overlaid with DSC curves and Raman spectra in the characteristic regions of the C═N and NCS$^-$ groups in the inset for **prF**.

2.1.3. Raman Spectroscopy

Variable temperature Raman spectra of **prF** during the heating process were recorded in the range of 100–2400 cm^{-1} (Figure 1, inset; Figure S2, Supporting Information). As in other Fe^{II} thiocyanate SCO complexes, the stretching vibration mode of NCS and C═N of Schiff base ligands show a clear spin-state correlation marker.[19] In the HS state, the two stretching vibration modes, attributable to the NCS$^-$ groups, are located at 2069 and 2103 cm^{-1}. The emergence of both modes may be induced by the crystal packing constraints and the correlated distortion of the coordination sphere of the two *trans* NCS$^-$-anions. However, these packing effects are clearly mitigated as the molecular volume shrinks in the LS state and only the high-frequency vibration mode is observed at 2106 cm^{-1}. The C═N stretching vibration mode in the HS state is located at 1616 cm^{-1}. Upon transition to the LS state, its intensity increases and it moves down to 1614 cm^{-1}. Compared to the magnetic results, the transition temperature ($T_{1/2}$ ≈263 K) obtained from Raman spectra is slightly lower, which can be attributed to the additional thermalization of the sample by laser irradiation and the difference in temperature sensors.

2.1.4. Single Crystal Structure

Following the magnetic and spectroscopic studies of **prF**, the crystal structure of the complex was analyzed in the LS and HS states. Compound **prF** shows the monoclinic $P2_1/c$ space group in both spin states at 120 K (LS) and 350 K (HS). Relevant crystal

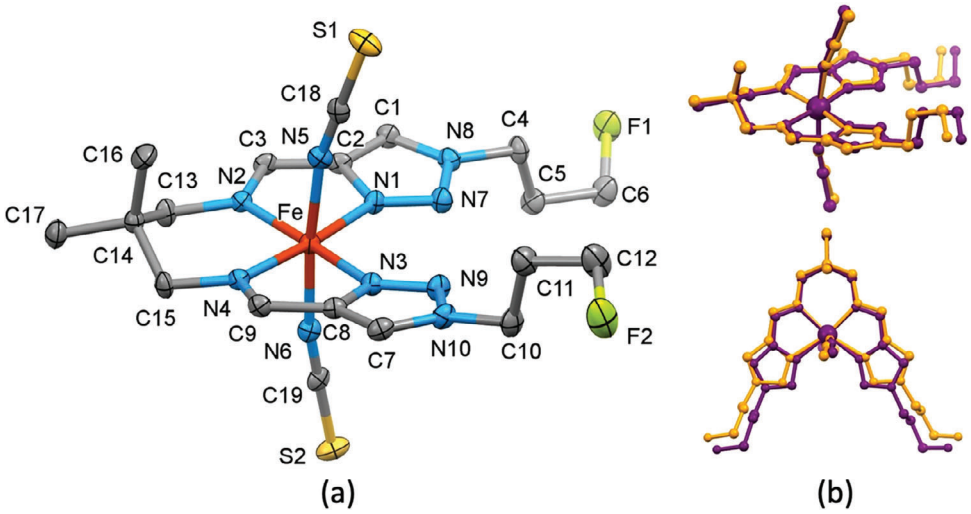

Figure 2. a) Molecular structure of **prF** (120 K) with thermal ellipsoids are represented at 50% probability. The hydrogen atoms are omitted for clarity; b) Minimized overlay, visualizing structural changes due to the SCO between the LS (purple) and HS (orange) spin states.

data are collected in Table S1 (Supporting Information), and the corresponding bond lengths and angles involving the $[Fe^{II}N_6]$ environment together with the corresponding average Fe—N bond length, <Fe—N>, are collected in Table S2 (Supporting Information). As usual in this family of compounds,[14c] the coordination sphere of the central ion is defined by a distorted $[FeN_6]$ octahedron with the tetradentate N_4 ligand occupying the equatorial positions and the two SCN^- ligands completing the axial *trans* positions. **Figure** 2a) displays the molecular structure of the compound together with the relevant atom numbering. The average Fe—N bond lengths and its change (1.969 Å (LS)/2.159 Å (HS), Δ<Fe—N> = 0.190 Å) upon SCO are perfectly consistent with the occurrence of a complete transition in agreement with the magnetic properties. The change of spin state is also reflected on the variation of the distortion indices. The average trigonal distortion parameters $\Sigma = \Sigma_1^{12}(|90 - \varphi_i|)$, φ_i is angle N—Fe—N',[20] and $\Theta = \Sigma_1^{24}(|60 - \theta_i|)$, θ_i is the angle generated by superposition of two opposite faces of the octahedron[21] are 53.38/84.08° and 189.80/333.01°, in the LS/HS states, respectively. The continuous shape measure[22] [CShM(O_h)] value relative to the ideal O_h symmetry changes from 0.723 to 2.270 due to the SCO. The minimized overlay of molecule **prF** visualizing geometric changes due to the SCO in two projections is shown in Figure 2b).

The crystal packing of **prF** is the same in the HS and LS states, with the molecules tightly packed in a head-to-head fashion along the *a* axis forming supramolecular 1D chains stacked in the *bc* plane with the segregated head groups and 1-fluoropropyl-groups in between (**Figure** 3a). The molecules within the chain are bound by weak hydrogen bonds CH···S between the capping diamine and thiocyanate anions of the neighbor molecules in both spin states (Figure 3b; Figure S3, Supporting Information), and tables therein). In the LS state, a denser network of hydrogen bonding is formed with the supramolecular chains additionally bound by interchain interactions CH···S/N involving the thiocyanate and triazole or aliphatic groups. On the other hand, in the HS the interchain hydrogen bonds are represented only by one CH···N interaction between triazole and aliphatic groups. Additionally, each molecule is involved in the formation of an intricate 3D network of short contacts involving X···H (X = F, S, C, and N) and C···F and C···N pairs close and/or smaller than the sum of the van der Waals radii that, as expected, most of them become shorter and their number increases when moving from the HS to the LS state (see Figure S3, Supporting Information).

2.1.5. Energy Framework Analysis

Understanding the relationship between the crystal structure and the physical properties of SCO complexes is a critical step in designing materials with desirable characteristics. The energy framework analysis is a new and convenient tool for evaluating the energetics of crystal structures and the SCO properties that arise from these structures.[23] In the method, centroids of molecules in the crystal structure are viewed as nodes connected by cylinders whose diameter is proportional to the magnitude of the interaction energy, which takes into account electrostatic, polarization, dispersion, and exchange-repulsion interaction contributions calculated using quantum mechanical methods based on B3LYP/6-31G(d,p) molecular wavefunctions (for details see the Supporting Information). By constructing energy difference framework (EDF) of the HS and the LS structures, it is possible to visualize changes in the interactions with the nearest neighboring surrounding resulting from changes in the molecular shape due to the SCO and the expansion/contraction of the lattice. The EDF enables identification of the molecule–molecule contacts that are the most affected on transformation of the molecule and provides insight into the pathways of the cooperativity.

The EDF of **prF** has a 3D character, as is shown in the projections of a lattice fragment in **Figure** 4. Out of eleven identified unique molecular pairs (Table S3, Supporting Information), interactions of eight ones are weakening with the positive change across the transition LS-to-HS lattice reaching 15.2 kJ mol^{-1}, while out of the three strengthening interactions the lowest value is −6.1 kJ mol^{-1}. The inconsistency in number and strength

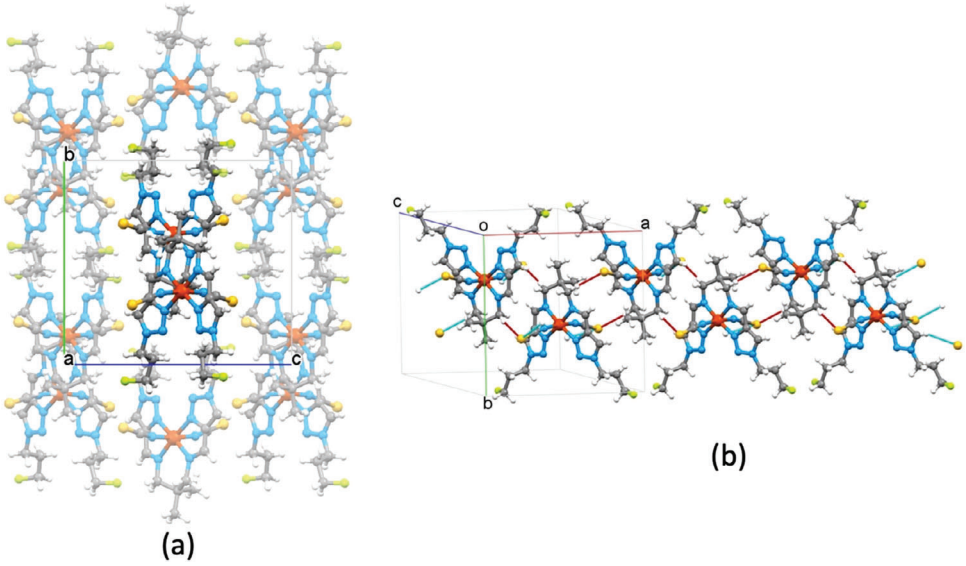

Figure 3. a) Crystal packing view of **prF** along the *a* axis with the highlighted repeated 1D-supramolecular chain where molecules are packed in a head-to-head fashion. b) The 1D supramolecular chain viewed perpendicular to the *a* axis with the weak hydrogen bonds C—H···S as red lines.

between the weakening and strengthening interaction makes it similar to low cooperativity SCO transition compounds of different types described by Reeves et al.[24] On opposite, a congener complex **pr** with unsubstituted propyl substituents, showing hysteresis *ca*. 14 K wide is characterized by a larger amplitude of the EDF energies, embracing values in the range –20.8–+ 25.1 kJ mol^{-1}.[14c] The nearly balanced energy change between the weakening and strengthening EDF interactions in the case of the propyl-substituted complex **pr** and the imbalance of the same in **prF** allows us to explain the different width of the hysteresis, which is wider for the larger amplitude of equal in strength but opposite in sign interaction energies of EDF, as described

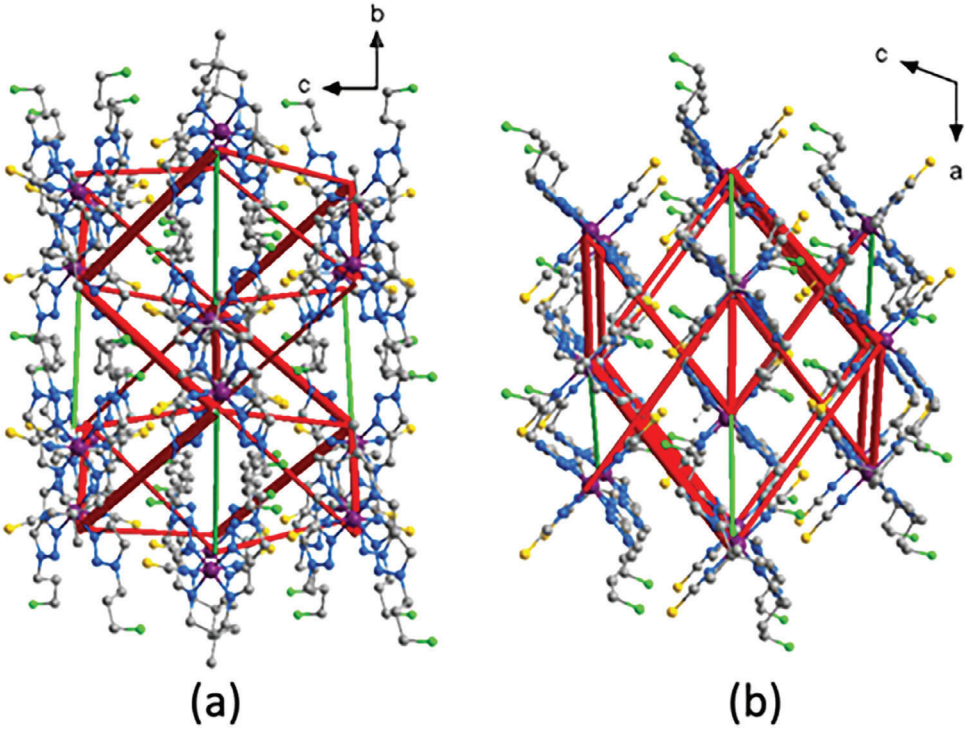

Figure 4. The EDF of **prF**, constructed using the values from the Table S3 (Supporting Information), column ΔE_{tot}(HS–LS), and superimposed on a fragment of the LS crystal lattice. The red cylinders correspond to the weakening interactions, the green cylinders to the strengthening interactions. Tube size is scaled proportionally to the absolute value of the interaction energy, cut-off is 5 kJ mol^{-1}.

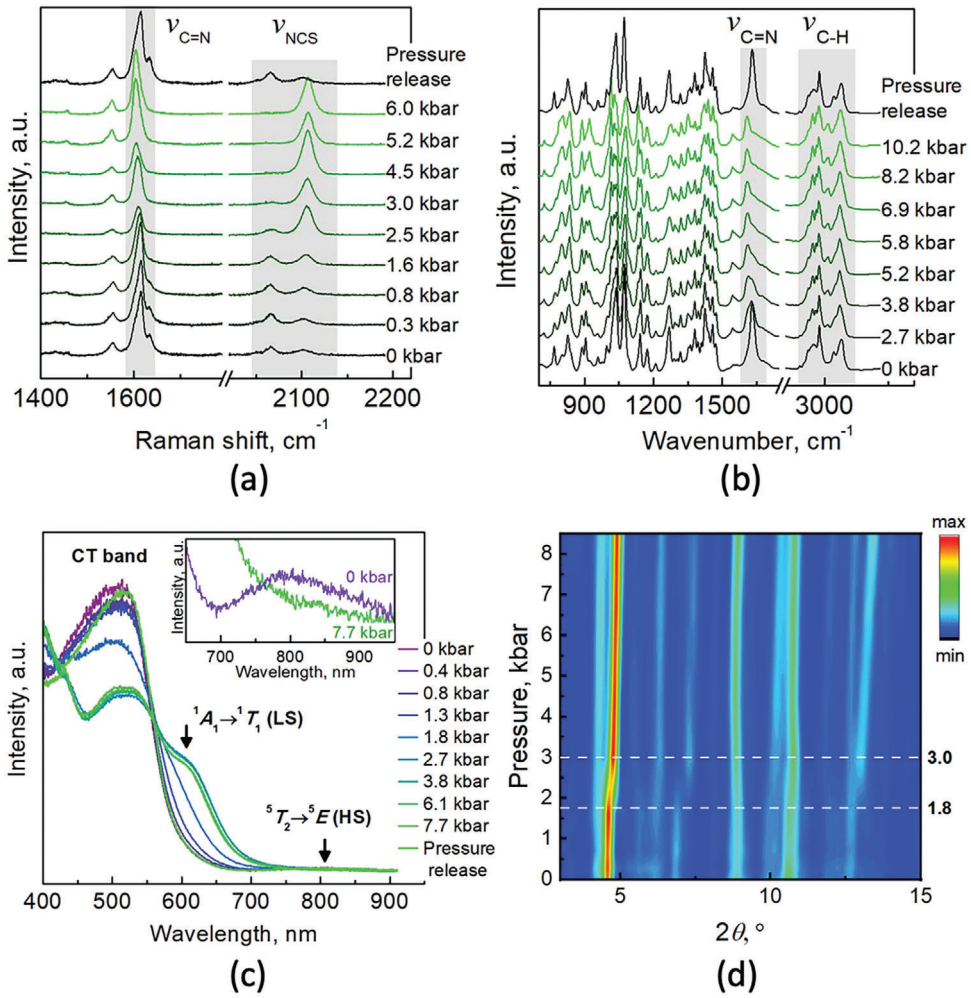

Figure 5. a) Variable pressure Raman spectrum of single crystal of **prF**; b) The IR absorption spectrum under pressure (the signals in the 1750–2700 cm^{-1} range are not considered because of the strong diamond bands at 2000–2500 cm^{-1}); c) Change of the UV–vis absorption spectrum of **prF** under pressure. The inset shows the detailed region of the weak d–d absorption peak $^5T_2 \rightarrow {}^5E$ at low- and high-pressure values; d) Contour diagram of the X-ray diffraction pattern in the characteristic range $2\theta = 3–15°$ under increasing pressure.

by Reeves et al.[24] The fluorination of the pendant propyl substituent changes the energy framework due to the F···C/H interactions, resulting in a global change of intermolecular interaction pattern and, consequently, a low hysteretic SCO behavior ideal for barocaloric applications.

2.2. Pressure-Induced SCO Behavior at Room Temperature and Barocaloric Properties

Since the BCE is directly related to the pressure-induced SCO, we have used UV–vis absorption spectroscopy,[25] Raman[26]/IR spectroscopies,[27] and powder X-ray diffraction[26] to explore the response of spin states to pressure at room temperature.

2.2.1. Raman and IR Spectroscopy under Pressure

The pressure dependence of the Raman spectrum of **prF** (**Figure 5a**) is similar to the above-described temperature-dependent Raman spectrum. In the HS state and at ambient pressure, the NCS^- stretching vibration modes appear at 2069 and 2103 cm^{-1} but above 2.5–3.0 kbar, the low-frequency mode disappears, while the intensity of the high-frequency one reaches a maximum value, indicating the complete SCO transition in this pressure range. In addition, the C═N stretching vibrations mode shifts to a lower frequency as the pressure increases.

Similar to Raman spectroscopy, in the IR spectra, the stretching vibration mode of C═N shifts toward lower wave numbers from 1630 to 1610 cm^{-1} when moving from 2.7 to 3.8 kbar respectively (Figure 5b). In addition, the stretching vibration mode of the C—H bonds also shows variations due to the large structural changes induced in the lattice caused by the SCO in the same pressure range. The higher range of SCO transitions compared to Raman measurements is due to the non-hydrostatic conditions, since KBr rather than liquid oil is used as the pressure transmitting medium.[28]

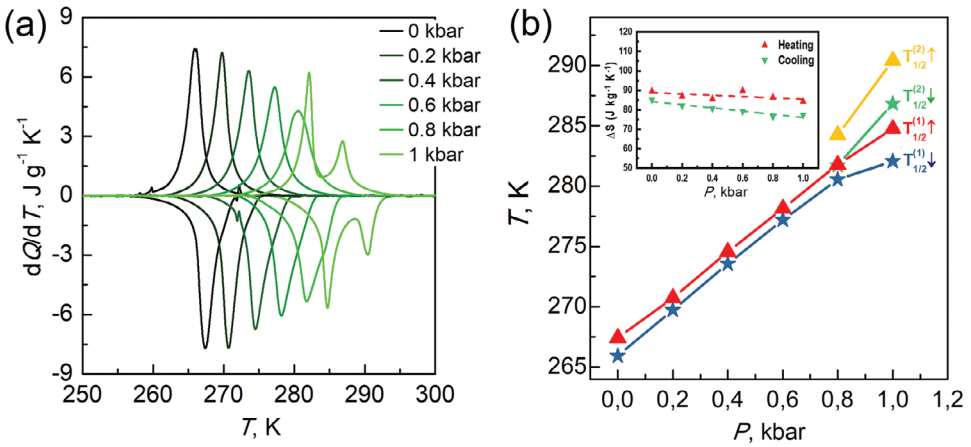

Figure 6. a) Temperature-dependent isobaric heat flow dQ/dT at different pressures, after subtracting the baseline. The upper and lower curves correspond to the exothermic peak of the HS to LS transition during cooling and the endothermic peak of the LS to HS transition during heating respectively. b) Transition temperature as a function of pressure. Below 0.8 kbar blue and red symbols correspond to HS→LS and LS→HS transitions, respectively, and above 0.8 kbar blue, red, green, and yellow symbols correspond to mS→LS, LS→mS, HS→mS, and mS→HS, transitions, respectively (the steps are calculated from room temperature). The inset shows the evolution of the isobaric entropy change associated with the SCO as a function of pressure. The integral range of isobaric entropy change is from T_{tr} – 7 K to T_{tr} + 7 K, where T_{tr} is the peak position of the latent heat peak.

2.2.2. UV–Vis Absorption Spectra

The evolution of UV–vis absorption spectra with pressure (Figure 5c) envisages the spin state change of the compound under pressure.[29] At ambient pressure, the characteristic low-intensity *d–d* absorption peak ($^5T_2 \rightarrow {}^5E$) typical for the HS Fe^{II} ion is observed at ≈800 nm. With the pressure increase, the absorption peak weakens and eventually disappears, while the intensity of the broad and complex charge-transfer (CT) band embracing the range 400–600 nm significantly increases. Particularly characteristic is the relatively strong absorption band at ≈630 nm, which appears abruptly at 1.3 kbar and reaches saturation at 2.7 kbar, and that was attributed to the $^1A_1 \rightarrow {}^1T_1$ transition of the Fe^{II} ion in the LS state.[30] This indicates that abrupt SCO occurs within this pressure range.

2.2.3. Powder X-Ray Diffraction (PXRD)

The variable pressure PXRD method was used to investigate the lattice parameters transformation under pressure-induced SCO. The contour plot of diffractogram as a function of pressure (Figure 5d) shows a discontinuous change in the position of diffraction peaks with increasing pressure, corresponding to the crystal structure change caused by the abrupt change of the spin state. The evolution of the unit cell parameters with increasing pressure is evaluated by indexing the X-ray diffraction patterns at each pressure value. Upon the HS-to-LS transition, the contraction of Fe—N bonds leads to the reduction of octahedral coordination environment and eventually causes the volume contraction and distortion of unit cell, clearly visible by the change of unit cell parameters in the interval of 1.8–3.0 kbar (Figure S4, Supporting Information). From the obtained data, the change in the unit cell volume due to SCO is estimated to be *ca.* 16 Å^3 (≈2.5%). This large change leads to a high sensitivity of the transition temperature ($T_{1/2}$) to external pressure, resulting in an easily observable reversible BCE of **prF** (vide infra).

Summarizing the results, it can be concluded that the pressure-induced SCO transition of **prF** at RT under hydrostatic conditions takes place in the pressure range 1.5–3.0 kbar, which is consistent with the extrapolation results from the calorimetric measurements under applied pressure, presented below. Also, all the methods used confirm the recovery of the initial HS state after pressure release.

2.2.4. Thermodynamic Behavior of *prF* Under Pressure

Although SCO is a purely molecular phenomenon and is determined by microscopic parameters, the relationship between microscopic and thermodynamic parameters of the transition under external stimuli[31] permits to describe it by thermodynamic parameters – changes in heat capacity, entropy, volume, and interaction energy. Therefore, in order to explore the potential of **prF** for applications in the barocaloric refrigeration, isobaric calorimetry measurements were performed at multiple hydrostatic pressures. The baseline-corrected heat flow curves $\frac{dQ}{dT}$ associated with the heating and cooling induced SCO at different pressures are shown in **Figure 6a**. Upon pressure increase, the exothermic and endothermic peaks related to the HS-LS and LS-HS transitions move up in temperature. This behavior is consistent with pressure favoring stabilization of the LS state with lower volume. The single latent heat peak associated with the HS↔LS transition shows a linear pressure dependence at pressures below 0.8 kbar, with $\frac{dT_{1/2}}{dP}$ of 18.0 ± 0.3 K kbar^{-1} for heating and 18.8 ± 0.1 K kbar^{-1} for cooling. These values are consistent with the result predicted by the Clapeyron equation $\frac{dT_{1/2}}{dP} = \frac{\Delta V}{\Delta S}$ = 19.4 K kbar^{-1}, where ΔV is derived from the structural data obtained under pressure (Figure S4, Supporting Information). The small hysteresis evaluated from the peak maxima is constant in this pressure range. At a pressure above 0.8 kbar, a

single peak of latent heat splits into two consecutive peaks, indicating the appearance of a new mixture state (mS) of HS and LS states. Two-step transition may be caused by the different compressibility of LS and HS complexes and the appearance of the inner inhomogeneity pressure or by structure transition.[32] By integrating the heat flow curve $\frac{1}{T}\frac{dQ}{|dT|}$ after subtracting the baseline, entropy changes under different pressures are evaluated and shown in the inset in Figure 6b. In the studied pressure range, the entropy change (ΔS) decreases with the pressure, which may be caused by pressure suppression of the vibration entropy away from SCO temperature[11d,33] It is worth noting that the entropy change $\Delta S = \Delta S^{HS\leftrightarrow mS} + \Delta S^{mS\leftrightarrow LS}$ above 0.8 kbar is essentially consistent with the entropy change $\Delta S = \Delta S^{HS\leftrightarrow LS}$ in the low pressure range. In addition, combined with the isobaric entropy changes of heating and cooling under multiple pressures (Figure S5, Supporting Information), $\Delta S^{HS\leftrightarrow IP} \approx \Delta S^{IP\leftrightarrow LS}$ at 1 kbar indicates that the transition profile of **prF** may change (single-step SCO to two-step SCO). Considering that in the case of a structural transition there should be a change in entropy, and in the experiment, we see only a change in entropy associated with the spin transition, we believe that the cause of the splitting of the latent heat peak is the influence of the internal inhomogeneous pressure.

2.2.5. BCE and Barocaloric Performance

Due to the challenge of strictly maintaining isothermal and adiabatic conditions in calorimetric experiments with variable pressure, we utilize the quasi-direct method to evaluate the BCE. The isobaric entropy, through and on each side of the transition, as a function of temperature and pressure was obtained with respect to the baseline value, S_0, initial temperature, T_0, and atmospheric pressure. For this purpose, we proceed as described in references [34] and assume that the specific heat of all states is independent of pressure:

$$S^*(T,P) = \begin{cases} S^*(T_0,P) + \int_{T_0}^{T} \frac{C_P^{LS}}{T} dT & T \le T_1 \\ S^*(T_1,P) + \int_{T_1}^{T} \frac{1}{T}\left(C_P + \frac{dQ}{dT}\right) dT & T_1 < T \le T_2 \\ S^*(T_2,P) + \int_{T_2}^{T} \frac{C_P^{HS}}{T} dT & T_2 < T \end{cases} \quad (1)$$

where T_1 and T_2 are the starting and ending temperatures of the SCO, respectively. C_P^{HS} and C_P^{LS} are the specific heat of the HS and LS states (Figure S6, Supporting Information), respectively, while $C_P = \gamma_{HS}\, C_P^{HS} + (1-\gamma_{HS}) C_P^{LS}$ is the specific heat in the SCO process, where γ_{HS} is the high spin fraction obtained by normalized isobaric entropy. Equation (1) can also be used for the two-step SCO processes. Due to the high compressibility of metalorganic materials, the contribution to entropy of the pressure dependence of specific heat below temperature T_0 should be considered.[5b,35] This part of the additional entropy, known as the elastic thermal contribution, is evaluated by the formula obtained from the Maxwell relation $(\frac{\partial V}{\partial T})_P = -(\frac{\partial S}{\partial P})_T$:

$$\Delta S_+ (P_f - P_i) = -\int_{P_i}^{P_f} \left(\frac{\partial V}{\partial T}\right) dP \quad (2)$$

The additional entropy change is due to the pressure offset of the entropy caused by thermal fluctuations. Assuming that the coefficient of thermal expansion of the material is independent of pressure, the extra entropy will be able to be expressed as follows.[11e,36]

$$\Delta S_+ = -\left[\left(\frac{\partial V}{\partial T}\right)_{P=0}\right] \Delta P = -(V \times \alpha) \times \Delta P \quad (3)$$

where V is the volume, $\alpha = (\frac{\partial \ln V}{\partial T})_{P=0}$ is the coefficient of thermal expansion at ambient pressure, and $\Delta P = P_f - P_i$ is the driving pressure. Here, P_i and P_f are the initial and final pressures of the process, respectively. Therefore, the isobaric entropy is expressed as $S_{ib}(T,P) = S^* + \Delta S_+$ after considering the effect of pressure on the specific heat.

Using the heat flow curves at different pressures, the specific heat data at atmospheric pressure and the coefficient of thermal expansion (referring to the studied thermal expansion coefficient considered in this paper for SCO compounds is assumed to be 2.5 10^{-4} K^{-1}),[11e,f] the isobaric entropy change $\Delta S_{ib}(T, P) = S_{ib}(T, P) - S_{ib}(T_0, P_{atm})$ referring to temperature T_0 = 240 K was obtained as a function of temperature and pressure. The isobaric entropy changes ΔS_{ib} for the heating and cooling processes are shown in **Figure** 7a,b, respectively. The isothermal entropy change (ΔS_{it}) and adiabatic temperature change ΔT_{ad}, which are important parameters for characterizing the BCE, can be directly obtained according to the isobaric entropy change curves at different pressures.

$$\Delta S_{it}(T, P_i \to P_f) = \Delta S_{ib}(T, P_f) - \Delta S_{ib}(T, P_i) \quad (4)$$

$$\Delta T_{ad}(T, P_i \to P_f) = T(\Delta S_{ib}, P_f) - T(\Delta S_{ib}, P_i) \quad (5)$$

For materials with typical BCE $(\frac{dT_{1/2}}{dP}) > 0$, compression corresponds to the exothermic process and decompression corresponds to the endothermic process. Thus, ΔS_{it} and ΔT_{ad} for the pressurization process are obtained from the curves for the cooling process, while ΔS_{it} and ΔT_{ad} for the decompression process are obtained from the curves for the heating process. ΔS_{it} and ΔT_{ad} of **prF** at different pressures are shown in Figure S7 (Supporting Information) as functions of temperature and starting temperature, respectively. The reversibility of solid materials with the BCE during pressure cycling is one of the key factors in the practical application of cooling devices. The reversible isothermal entropy change $\Delta S_{it,rev}(0\leftrightarrow P)$ is obtained by the overlap of $\Delta S_{it}(T,0 \to P)$ and $\Delta S_{it}(T,P \to 0)$. (Figure 7c). The adiabatic reversible temperature change is calculated according to the equation $|\Delta T_{ad,rev}(T, 0\leftrightarrow P)| = |T(\Delta S_{ib,cooling}, P) - T(\Delta S_{ib,heating}, 0)|$ (Figure 7d). Due to the small hysteresis width and a high-pressure sensitivity, compound **prF** shows a large reversible BCE under lower pressure. The values $\Delta S_{it,rev,max}$, $\Delta T_{ad,rev,max}$, and RC_{rev} are plotted as functions of pressure in Figure 7e,f, where RC

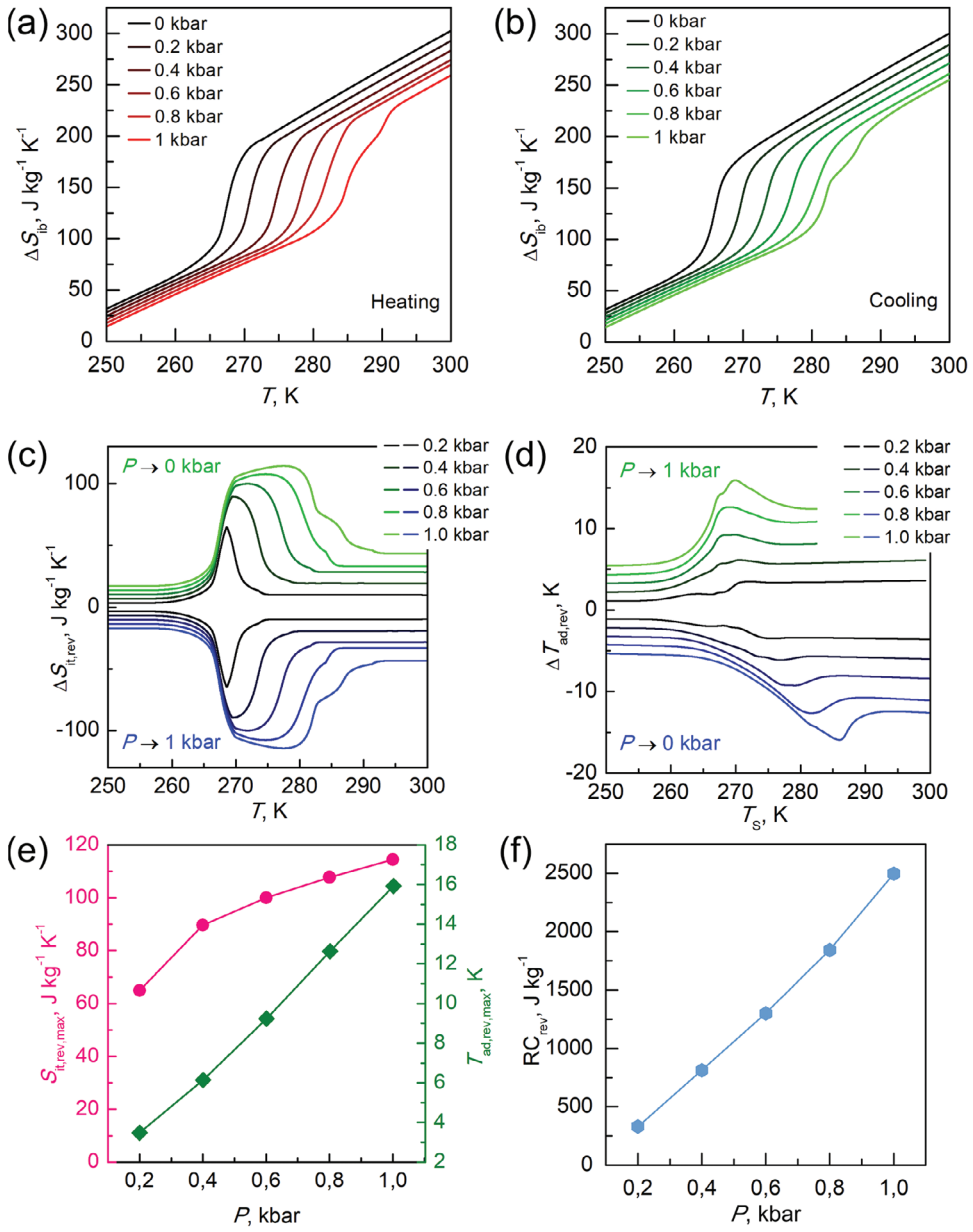

Figure 7. Temperature-dependent isobaric entropy curves at different pressures on a) cooling and b) heating; c) Reversible isothermal entropy change ($\Delta S_{it,rev}$) as a function of temperature at different pressures. d) Reversible adiabatic temperature change ($\Delta T_{ad,rev}$) at different pressures as a function of the starting temperature. e) Maximum reversible isothermal entropy changes ($\Delta S_{it,rev,max}$) and adiabatic temperature change ($\Delta T_{ad,rev,max}$) as a function of operating pressure. f) Reversible refrigeration capacity (RC_{rev}) as a function of operating pressure.

is an important parameter that characterizes the refrigerant capacity of the material.[6a,37] At 1 kbar, **prF** exhibits the colossal BCE with $\Delta S_{it,rev} \approx 114.43$ J kg^{-1} K^{-1} and $\Delta T_{ad,rev} \approx 15.92$ K. Moreover, at this pressure it exhibits excellent refrigerant performance, $RC \equiv \int \Delta S_{it,rev} dT \approx 2496$ J kg^{-1}, which is comparable or exceeds the performance of the excellent barocaloric materials previously studied: $(C_{10}H_{21}NH_3)_2MnCl_4$ (RC ≈ 3500 J kg^{-1}, 1 kbar),[34a] C_{60} (RC ≈ 500 J kg^{-1}, 1 kbar),[34a] $(NH_4)_2SO_4$ (RC ≈ 276 J kg^{-1}, 1 kbar),[36] Mn_3GaN (RC ≈ 125 J kg^{-1}, 0.9 kbar),[38] TMA (RC ≈ 1701 J kg^{-1}, 0.9 kbar).[39] In addition to the excellent BCE of **prF**, its region of operation is near the freezing point of water, indicating that it can be used in domestic refrigerators. In order to evaluate the refrigeration efficiency of a material during the refrigeration process, the coefficient of refrigerant performance (CRP),[40] defined as $CRP = |\frac{\Delta S_{it,rev,max} \times \Delta T_{ad,rev,max}}{W}|$ has been calculated. Here W is the mechanical work required to drive a reversible refrigeration cycle, which is calculated as $W = 1/2P\Delta V$. At $P = 1$ kbar, CRP of **prF** is estimated as 1.99 ± 0.10, which is close to the maximum possible value and higher than in any SCO barocaloric materials previously reported. In Table S4 (Supporting Information), the thermodynamic properties of the title compound (transition temperature, hysteresis width,

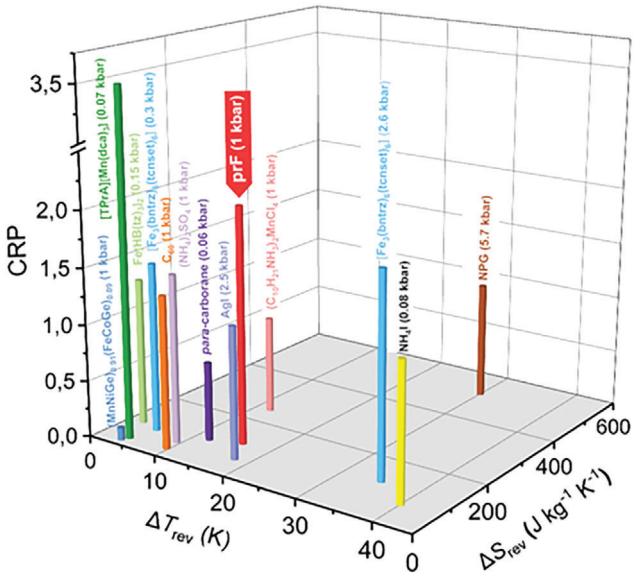

Figure 8. The refrigerant performance coefficient (CRP), reversible adiabatic temperature change, and reversible isothermal entropy change of different materials reported in the literature (see Table S5, Supporting Information) together with the data of **prF** at1 kbar.

entropy change, and pressure sensitivity of the transition temperature) are compared with the known Fe^{II} SCO compounds for that the BCE has been investigated. The small hysteresis loop width, large entropy change, and high-pressure sensitivity indicate that the title compound is an excellent solid cooling material with low driving pressure.

As shown in **Figure 8** and Table S5 (Supporting Information), compound **prF** has high cooling efficiency and strong cooling capacity due to the high adiabatic transition temperature change. The excellent BCE is exhibited at low pressures, which opens perspectives for the practical application as a barocaloric material. Since the properties of SCO compounds can be regulated by modification of ligands to adapt to the temperature range required for application, our results will further stimulate research on SCO compounds in solid-state refrigeration. As is shown in this work, it is possible to rationally design Fe^{II} SCO compound by adjusting hysteresis width with subtle modifications of the peripheral aliphatic chains.

3. Conclusion

In SCO complexes, the change in the spin state of the Fe^{II} center serves as a trigger for larger-scale molecular and lattice changes that determine the thermodynamic properties of the material. Although from a general point of view the task of designing complexes with high SCO entropy change is not straightforward, a gentle modification of the intermolecular contact of the peripheral groups of a hysteretic compound can be an acceptable strategy. We have demonstrated in this work, that terminal fluorination of the pendant propyl groups of the hysteretic material affords an Fe^{II} complex with a low-hysteretic high entropy SCO behavior just below the RT. The obtained compound **prF** exhibits a reversible colossal isothermal entropy change of ≈114 J kg^{-1} K^{-1} and a reversible adiabatic temperature change of ≈16 K at a driving pressure of 1 kbar, demonstrating an exceptionally high refrigerant performance coefficient compared to other solid-state and SCO materials. The reason for this significant pressure response is the relatively large volume change associated with the molecular and intermolecular rearrangements during the SCO event, as suggested by the performed exhaustive studies. The title compound demonstrates the potential that SCO compounds can offer to the search for advanced functional materials with barocaloric properties, as the right choice of ligand can dramatically affect the BCE, and therefore there remains ample opportunity to explore other SCO materials with even more intriguing properties. We expect that the here reported results to stimulate further investigations into the BCE and shed light to the design principles that can lead to resilient abrupt non-hysteretic SCO behavior at required temperature, with a significant volume variation allowing low driving pressure. In our opinion, the search should be continued among low molecular weight neutral complexes with peripheral groups prone to display order-disorder structural transitions (pendant or bridging aliphatic, halogenated aliphatic), which can additionally contribute to the entropy- and volume variation across the SCO transition.

4. Experimental Section

Materials: All chemicals were purchased from commercial suppliers and used without further purification (Aldrich, Enamine). Complex $[Fe(py)_4(NCS)_2]$ was synthesized following the method reported in the literature.[41]

Synthesis of 1-(3-Fluoropropyl)−1H-1,2,3-Triazole-4-Carbaldehyde: This aldehyde was synthesized following a modified protocol by Fletcher et al.[16] (**Scheme 2**). To a 100 mL flask was added $CuSO_4$ (0.32 g, 2 mmol), L-ascorbic acid sodium salt (0.79 g, 4 mmol), water (40 mL), *t*-butyl alcohol (40 mL), 1-azido-3-fluoropropane (1.0 g, 9.7 mmol) and propargyl aldehyde diethyl acetal (1.57 mL, 11 mmol). The vial was then capped and stirred at 70 °C overnight. To the reaction mixture was then added 5% NH_4OH (aq) (50 mL) and the suspension repeatedly extracted by $CHCl_3$ (3 × 50 mL). The organic extracts were combined, dried over $MgSO_4$, and filtered through a paper filter. The solvent was removed by rotary evaporation to yield a brown-orange product (≈1.1 g), which was used for NMR spectroscopic study and GC, and whose purity was estimated at 80%. No further purification was performed. ^{1}H NMR (300 MHz, $CDCl_3$): δ 10.27 (1H, s, CHO), 8.12 (1H, s, CH^{trz}), 4.59 (2H, t, J = 6.8 Hz, and NCH_2), 4.46 (2H, dt, J^1 = 53.0 Hz, J^2 = 5.2 Hz, and CH_2F), 2.35 (2H, dt, J^1 = 26.6 Hz, J^2 = 6.1 Hz, and CH_2). MS ESI m/z (rel. int.): theor. calcd 157.1 [M+] (100.0%). Found 158.0 [M+H+] (100.0%).

*Synthesis of **prF***: To a boiling solution of $[Fe(py)_4(NCS)_2]$ (100 mg, 0.2 mmol) and excess of the crude 1-(3-fluoropropyl)−1*H*-1,2,3-triazole-4-carbaldehyde (≈40 mg) in MeOH (10 mL), 2,2-dimethylpropane-1,3-diamine (24 µL) was added (Scheme 2). The orange-brown solution formed was quickly filtered while hot through a plug of cotton and left overnight at room temperature. The needle-like red crystals formed were filtered off, dried with cold methanol, and air dried. Yield 65 mg, 59%. Elemental analysis calcd (%) for $C_{19}H_{26}F_2FeN_{10}S_2$: C, 41.31; H, 4.74; N, 25.35. Found: C, 41.58; H, 4.55; N, 25.65.

Variable-Temperature Magnetic Susceptibility Data: These data were recorded on a sample of **prF** (15 mg) at 1 K min^{-1} rate between 10 and 400 K using a Quantum Design MPMS2 SQUID susceptometer operating at 1 T magnetic field. Elemental CHN analysis was performed after combustion at 850 °C using IR detection and gravimetry by means of a Perkin–Elmer 2400 series II device.

Single Crystal X-Ray Diffraction Data: These data were collected on a Nonius Kappa-CCD single crystal diffractometer using graphite

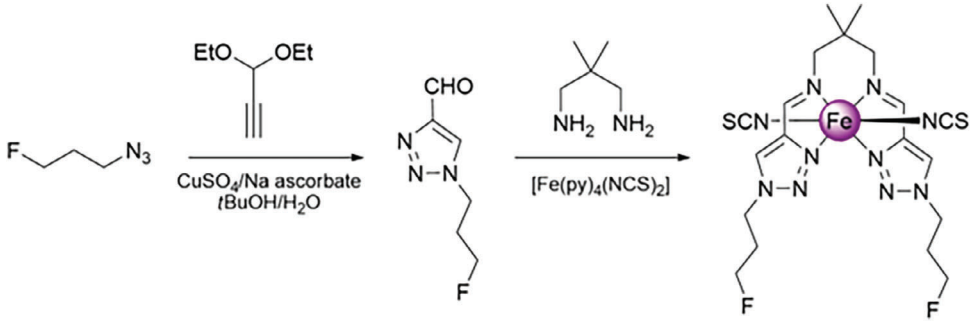

Scheme 2. Synthesis of **prF**.

mono-chromated Mo K_α radiation (λ = 0.71073 Å). A multi-scan absorption correction was performed. The structures were solved by direct methods using SHELXS-2014 and refined by full-matrix least squares on F^2 using SHELXL-2014.[42] Non-hydrogen atoms were refined anisotropically and hydrogen atoms were placed in calculated positions refined using idealized geometries (riding model) and assigned fixed isotropic displacement parameters. CCDC files, 2310141 and 2310142 contain the supplementary crystallographic data for this paper. These data can be obtained free of charge from The Cambridge Crystallographic Data Centre via www.ccdc.cam.ac.uk/data_request/cif.

Energy Framework Analysis Calculations: These calculations were performed by using *CrystalExplorer21*.[23b] Electrostatic potential and intermolecular interaction energies, which were partitioned into electrostatic, polarization, dispersion, and repulsion energy components, were calculated based on the B3LYP/6-31G(d,p) wave functions that were obtained by using the structural data from the corresponding CIF files. The obtained interaction energies were further utilized to map the network of energy frameworks across different pairs as cylinders connecting centroids of molecules, which radii were proportional to the strength of the corresponding intermolecular interactions.

Differential Scanning Calorimetric Under Pressure (HP-DSC): Heat flow data as a function of temperature and pressure were collected using a high-pressure differential scanning calorimeter (μDSC7, Setaram). About 20 mg of samples were sealed in a high-pressure vessel made of Hastelloy alloy. Hydrostatic pressures of up to 1 kbar in the high-pressure vessel were achieved by compressed nitrogen and precisely controlled through the high-pressure panel. Constant pressure scans were performed on a sample at 0, 0.2, 0.4, 0.6, 0.8, and 1 kbar at a rate of 1 K min^{-1}, respectively.

Specific Heat Measurement: Measurements of specific heat (C_p) were performed on a commercial differential scanning calorimeter NETZSCH DSC 200F3 Maia under ambient pressure at a rate of 5 K min^{-1}. The C_p values were obtained by the sapphire comparison method.

Variable Temperature Raman Spectroscopy: Raman spectra were measured with the Horiba Jobin Yvon HR800 confocal spectrometer, using a 532 nm laser as the excitation source. The Raman signal was recorded by a Princeton Instruments CCD detector and collected in the frequency range of 100–2400 cm^{-1}. The Rayleigh scattering was removed using a holographic notch filter. In order to avoid laser damage to the sample or the formation of local heat at the laser focus that affects the true temperature of the sample, the intensity of excitation light is <1 mW. The temperature control of the variable temperature process was performed by the temperature control platform LINKAM THMS600/TMS94. The temperature was stabilized for 5 min before each temperature point was measured to keep the temperature even and accurate.

UV–Vis Absorption Spectra Under High Pressure: The absorption spectrum of the sample under hydrostatic pressure was measured by the Ocean Optics QE65 Pro scientific research spectrometer. Diamond anvil cell composed of a pair of II-type diamonds was used as a pressure generating device. A single crystal of moderate thickness was placed in a pressure chamber composed of a drilled stainless-steel gasket, and silicone oil was used as a pressure transmitting medium. The pressure in the sample chamber was calibrated by the pressure dependence of the ruby's fluorescence emission.

Raman Spectroscopy Under Pressure: Raman spectra at high pressure were measured with the Horiba Jobin Yvon HR800 confocal spectrometer. The excitation source was a 532 nm laser. Diamond anvil cell composed of low fluorescent I-type diamond was adopted, and silicone oil was used as the pressure transmission medium.

High Pressure Infrared Spectroscopy: In situ high-pressure infrared spectra in the range of 3500–600 cm^{-1} were measured on the Bruker spectrometer (VERTEX 80v). Diamond anvil cell composed of a pair of II-type diamonds was used as a pressure generating device. Potassium bromide (KBr) as a pressure transfer medium. KBr should be dried before each experiment to avoid the influence of the vibration pattern of water molecules.

Powder X-Ray Diffraction Under Hydrostatic Pressure: The polycrystalline sample was loaded into a diamond anvil cell (DAC) for the experiment. High-pressure X-ray diffraction data were obtained using graphite monochromated Mo-k_α radiation (λ = 0.71073 Å) on Rigaku Synergy Custom FR-X Diffractometer equipped with a Hybrid Photon Counting (HPC) X-ray detector (HyPix-6000HE). The CrysAlis software package was used for data collection and initial data reduction. Rietveld refinement was performed using GSAS software to obtain the evolution of unit cell parameters with pressure.

Supporting Information

Supporting Information is available from the Wiley Online Library or from the author.

Acknowledgements

M.S. and R.L. contributed equally to this work. M.S. and K.Z. acknowledge the support by the Ministry of Education and Science of Ukraine (Grant nos. 22BF037-03, 22BF037-04, and 24BF037-03). F.J.V.M. acknowledges the support of the European Social Fund (ESF) and Generalitat Valenciana for his postdoctoral fellowship (APOSTD/2021/359). M.C.M. and J.A.R. thank the support given by the Spanish Ministerio de Ciencia e Innovación (grant PID2019-106147GB-I00 funded by MCIN/AEI/10.13039/501100011033). B.L. and Z.Z. acknowledge the support provided by the Ministry of Science and Technology of China grants (2022YFE0109900) and (2023JH6/100500003) and the Key Research Program of Frontier Sciences of Chinese Academy (Grant no. ZDBS-LY-JSC002). The authors are grateful to Dr. S. Malinkin for help with organic synthesis.

Conflict of Interest

The authors declare no conflict of interest.

Data Availability Statement

The data that support the findings of this study are available from the corresponding author upon reasonable request.

Keywords

barocaloric effect, calorimetry, iron(II) complexes, spin crossover, spin transition

Received: December 5, 2023
Revised: March 7, 2024
Published online: April 5, 2024

[1] Z. Zhang, X. Jiang, T. Hattori, X. Xu, M. Li, C. Yu, Z. Zhang, D. Yu, R. Mole, S.-i. Yano, *Mater. Horiz.* **2023**, *10*, 977.
[2] L. W. Davis, P. J. Gertler, *Proc. Natl. Acad. Sci. USA* **2015**, *112*, 5962.
[3] M. O. McLinden, J. S. Brown, R. Brignoli, A. F. Kazakov, P. A. Domanski, *Nat. Commun.* **2017**, *8*, 14476.
[4] M. O. McLinden, C. J. Seeton, A. Pearson, *Science* **2020**, *370*, 791.
[5] a) I. Takeuchi, K. Sandeman, *Phys. Today* **2015**, *68*, 48; b) X. Moya, N. Mathur, *Science* **2020**, *370*, 797.
[6] a) K. Gschneidner Jr, V. K. Pecharsky, *Annu. Rev. Mater. Sci.* **2000**, *30*, 387; b) L. Mañosa, A. Planes, *Adv. Mater.* **2017**, *29*, 1603607; c) J. Shi, D. Han, Z. Li, L. Yang, S.-G. Lu, Z. Zhong, J. Chen, Q. Zhang, X. Qian, *Joule* **2019**, *3*, 1200; d) R. Wang, S. Fang, Y. Xiao, E. Gao, N. Jiang, Y. Li, L. Mou, Y. Shen, W. Zhao, S. Li, *Science* **2019**, *366*, 216; e) H. Hou, S. Qian, I. Takeuchi, *Nat. Rev. Mater.* **2022**, *7*, 633.
[7] D. Boldrin, *Appl. Phys. Lett.* **2021**, *118*, 170502.
[8] a) M. S. Reis, *Coord. Chem. Rev.* **2020**, *417*, 213357; b) P. Lloveras, J.-L. Tamarit, *MRS Energy Sustain.* **2021**, *8*, 3; c) L. Cirillo, A. Greco, C. Masselli, *Therm. Sci. Eng. Prog.* **2022**, *33*, 101380.
[9] G. Levchenko, A. Khristov, V. Varyukhin, *Low Temp. Phys.* **2014**, *40*, 571.
[10] T. Hess, L. M. Maier, N. Bachmann, P. Corhan, O. Schäfer-Welsen, J. Wöllenstein, K. Bartholomé, *J. Appl. Phys.* **2020**, *127*, 075103.
[11] a) K. G. Sandeman, *APL Mater.* **2016**, *4*, 111102; b) P. von Ranke, *Appl. Phys. Lett.* **2017**, *110*, 181909; c) P. Von Ranke, B. Alho, R. Ribas, E. Nobrega, A. Caldas, V. De Sousa, M. Colaço, L. F. Marques, D. L. Rocco, P. Ribeiro, *Phys. Rev. B* **2018**, *98*, 224408; d) S. P. Vallone, A. N. Tantillo, A. M. dos Santos, J. J. Molaison, R. Kulmaczewski, A. Chapoy, P. Ahmadi, M. A. Halcrow, K. G. Sandeman, *Adv. Mater.* **2019**, *31*, 1807334; e) M. Romanini, Y. Wang, K. Gürpinar, G. Ornelas, P. Lloveras, Y. Zhang, W. Zheng, M. Barrio, A. Aznar, A. Gràcia-Condal, *Adv. Mater.* **2021**, *33*, 2008076; f) J. Seo, J. D. Braun, V. M. Dev, J. A. Mason, *J. Am. Chem. Soc.* **2022**, *144*, 6493; g) K. G. Sandeman, M. A. Halcrow, in *Barocaloric Effects in the Solid State* (Ed.: P. L. loveras), IOP Publishing, Bristol, UK **2023**, 1-5.
[12] a) M. Sorai, S. Seki, *J. Phys. Soc. Jpn.* **1972**, *33*, 575; b) G. Molnar, V. Niel, A. B. Gaspar, J. A. Real, A. Zwick, A. Bousseksou, J. J. McGarvey, *J. Phys. Chem. B* **2002**, *106*, 9701.
[13] P. Guionneau, M. Marchivie, G. Chastanet, *Chemistry* **2020**, *27*, 1483.
[14] a) H. Hagiwara, S. Okada, *Chem. Commun.* **2016**, *52*, 815; b) H. Hagiwara, T. Masuda, T. Ohno, M. Suzuki, T. Udagawa, K.-i. Murai, *Cryst. Growth Des.* **2017**, *17*, 6006; c) M. Seredyuk, K. Znovjyak, F. J. Valverde-Muñoz, M. C. Muñoz, V. M. Amirkhanov, I. O. Fritsky, J. A. Real, *Inorg. Chem.* **2023**, *62*, 9044.
[15] a) K. Znovjyak, M. Seredyuk, S. O. Malinkin, S. Shova, L. Soliev, *Acta Crystallogr.* **2020**, *76*, 1661; b) K. Znovjyak, M. Seredyuk, S. O. Malinkin, I. O. Golenya, V. M. Amirkhanov, S. Shova, N. U. Mulloev, *Acta Crystallogr.* **2021**, *77*, 573; c) K. Znovjyak, M. Seredyuk, S. O. Malinkin, I. A. Golenya, T. Y. Sliva, S. Shova, N. U. Mulloev, *Acta Crystallogr.* **2021**, *77*, 495.
[16] J. T. Fletcher, J. A. Christensen, E. M. Villa, *Tetrahedron Lett.* **2017**, *58*, 4450.
[17] P. Gütlich, A. Hauser, H. Spiering, *Angew. Chem., Int. Ed.* **1994**, *33*, 2024.
[18] C. P. Slichter, H. G. Drickamer, *J. Chem. Phys.* **1972**, *56*, 2142.
[19] K. Nakamoto, *Infrared and Raman Spectra of Inorganic and Coordination Compounds, Part B: Applications in Coordination, Organometallic, and Bioinorganic Chemistry*, 6th ed, John Wiley & Sons, Hoboken, NJ, USA **2009**.
[20] M. G. B. Drew, C. J. Harding, V. McKee, G. G. Morgan, J. Nelson, *J. Chem. Soc., Chem. Commun.* **1995**, 1035.
[21] H. R. Chang, J. K. McCusker, H. Toftlund, S. R. Wilson, A. X. Trautwein, H. Winkler, D. N. Hendrickson, *J. Am. Chem. Soc.* **1990**, *112*, 6814.
[22] L. J. Kershaw Cook, R. Mohammed, G. Sherborne, T. D. Roberts, S. Alvarez, M. A. Halcrow, *Coord. Chem. Rev.* **2015**, *289*, 2.
[23] a) M. J. Turner, S. P. Thomas, M. W. Shi, D. Jayatilaka, M. A. Spackman, *Chem. Commun.* **2015**, *51*, 3735; b) P. R. Spackman, M. J. Turner, J. J. McKinnon, S. K. Wolff, D. J. Grimwood, D. Jayatilaka, M. A. Spackman, *J. Appl. Crystallogr.* **2021**, *54*, 1006.
[24] M. G. Reeves, E. Tailleur, P. A. Wood, M. Marchivie, G. Chastanet, P. Guionneau, S. Parsons, *Chem. Sci.* **2021**, *12*, 1007.
[25] A. Hauser, in *Spin Crossover in Transition Metal Compounds I*, Topics in Current Chemistry, Vol. *233* (Eds.: P. Gütlich, H.A. Goodwin), Springer, NY, USA **2004**, p. 49.
[26] R. Li, G. Levchenko, F. J. Valverde-Muñoz, A. B. Gaspar, V. V. Ivashko, Q. Li, B. Liu, M. Yuan, H. Fylymonov, J. A. Real, *Inorg. Chem.* **2021**, *60*, 16016.
[27] R. Li, G. Levchenko, F. J. Valverde-Muñoz, A. B. Gaspar, V. V. Ivashko, Q. Li, W. Xu, H. Fylymonov, B. Liu, J. A. Real, *J. Mater. Chem. C* **2022**, *10*, 11388.
[28] R. Li, G. Levchenko, C. Bartual-Murgui, H. Fylymonov, W. Xu, Z. Liu, Q. Li, B. Liu, J. A. Real, *Inorg. Chem.* **2023**, *63*, 1214.
[29] G. Levchenko, G. V. Bukin, S. A. Terekhov, A. B. Gaspar, V. Martínez, M. C. Muñoz, J. A. Real, *J. Phys. Chem. B* **2011**, *115*, 8176.
[30] A. Hauser, in *Spin Crossover in Transition Metal Compounds II* (Eds: P. Gütlich, H. A. Goodwin), Springer, NY, USA **2004**.
[31] G. Levchenko, A. Khristov, V. Kuznetsova, V. Shelest, *J. Phys. Chem. Solids* **2014**, *75*, 966.
[32] a) D. Chernyshov, M. Hostettler, K. W. Törnroos, H. B. Bürgi, *Angew. Chem., Int. Ed.* **2003**, *42*, 3825; b) M. Griffin, S. Shakespeare, H. J. Shepherd, C. J. Harding, J. F. Létard, C. Desplanches, A. E. Goeta, J. A. Howard, A. K. Powell, V. Mereacre, *Angew. Chem., Int. Ed.* **2011**, *50*, 896; c) M. Paez-Espejo, M. Sy, K. Boukheddaden, *J. Am. Chem. Soc.* **2016**, *138*, 3202; d) M. Ndiaye, K. Boukheddaden, *Phys. Chem. Chem. Phys.* **2022**, *24*, 12870; e) R. Li, V. M. Kalita, H. Fylymonov, W. Xu, Q. Li, J. A. Real, B. Liu, G. Levchenko, *Inorg. Chem.* **2022**, *61*, 14752.
[33] A. Aznar, P. Lloveras, J. Y. Kim, E. Stern-Taulats, M. Barrio, J. L. Tamarit, C. F. Sánchez-Valdés, J. L. Sanchez Llamazares, N. D. Mathur, X. Moya, *Adv. Mater.* **2019**, *31*, 1903577.
[34] a) J. Li, D. Dunstan, X. Lou, A. Planes, L. Mañosa, M. Barrio, J.-L. Tamarit, P. Lloveras, *J. Mater. Chem. A* **2020**, *8*, 20354; b) J. Li, M. Barrio, D. J. Dunstan, R. Dixey, X. Lou, J. L. Tamarit, A. E. Phillips, P. Lloveras, *Adv. Funct. Mater.* **2021**, *31*, 2105154.
[35] A. Aznar, P. Lloveras, M. Barrio, P. Negrier, A. Planes, L. Mañosa, N. D. Mathur, X. Moya, J.-L. Tamarit, *J. Mater. Chem. A* **2020**, *8*, 639.
[36] P. Lloveras, E. Stern-Taulats, M. Barrio, J.-L. Tamarit, S. Crossley, W. Li, V. Pomjakushin, A. Planes, L. Mañosa, N. Mathur, *Nat. Commun.* **2015**, *6*, 8801.
[37] M. E. Wood, W. H. Potter, *Cryogenics* **1985**, *25*, 667.

[38] D. Matsunami, A. Fujita, K. Takenaka, M. Kano, *Nat. Mater.* **2015**, *14*, 73.
[39] A. Salvatori, D. Aguilà, G. Aromí, L. Mañosa, A. Planes, P. Lloveras, L. C. Pardo, M. Appel, G. F. Nataf, F. Giovannelli, *J. Mater. Chem. A* **2023**, *11*, 12140.
[40] a) L. D. Griffith, Y. Mudryk, J. Slaughter, V. K. Pecharsky, *J. Appl. Phys.* **2018**, *123*, 034902; b) E. Brück, H. Yibole, L. Zhang, *Philos. Trans. R. Soc., A* **2016**, *374*, 20150303.
[41] R. M. Golding, K. F. Mok, J. F. Duncak, *Inorg. Chem.* **1966**, *5*, 774.
[42] G. Sheldrick, *Acta Crystallogr.* **2015**, *71*, 3.